Proton Total Reaction Cross Sections for 22 Isotopes of Ti, Fe, Ni, Cu, Zn, Zr, and Sn at 14.5 MeV*

J. F. DICELLO,† G. J. IGO, AND M. L. ROUSH‡
Los Alamos Scientific Laboratory, University of California, Los Alamos, New Mexico
(Received 21 November 1966)

Total proton reaction cross sections have been measured at 14.5 MeV for 22 separated isotope targets to an accuracy of ±2% for Ti, Fe, Ni, Cu, Zn, and Zr isotopes and ±4½% for the Sn isotopes. A beam-attenuation technique employing a solid-state counter to detect elastically scattered protons at forward angles has been used. Use of the solid-state detector reduces the corrections due to inelastic processes to a negligible level. The total reaction cross sections for the Fe, Ni, Zn, and Zr isotopes increase more rapidly with increasing N than optical-model calculations based on 14.5-MeV elastic-scattering and polarization data predict. The measured values for Fe, Ni, Cu, Zn, and Zr isotopes were generally smaller than the optical-model predictions; the measured Sn values, however, were larger. The dip in σ_R near Ni, previously observed using elemental targets in a number of experiments, is reproduced by suitable averaging of the isotope reaction cross sections. The dip is shown to arise from a combination of a sharply rising σ_R with increasing N (for constant Z) and the relatively small average value of N for Ni due to shell closure.

I. INTRODUCTION

IT has become quite clear recently that 10–20 MeV proton total reaction cross-section measurements are essential in optical-model studies. Earlier analyses, usually based on elastic-scattering $d\sigma/d\Omega(\theta)$ data or on a limited, additional amount of polarization $P(\theta)$ data, predicted small differences in σ_R among the phenomenological families heretofore investigated.[1–3] A recent analysis[4] of comprehensive $d\sigma/d\Omega(\theta)$ and $P(\theta)$ data near 10 MeV requires nine parameters describing the central and spin-orbit potentials to be varied independently. This is so in order to obtain sufficient absorption of the incoming wave before the spin-orbit potential is encountered. The value of the total reaction cross section σ_R is related to the extent of the imaginary potential or alternatively the radius of the spin-orbit potential.

To be generally useful the accuracy of σ_R measurements must be 2–3%. Systematic measurements involving a large number of single isotope targets over a broad energy range are useful in studying isotopic-spin and energy-dependence effects. Equally important, σ_R must be accompanied by $d\sigma/d\Omega(\theta)$ and $P(\theta)$ data. Data from the (p,d) reaction will be useful when J-dependent effects are better understood.[4]

Data at 14.5 MeV (including the present σ_R measurements) on 22 single isotope targets cover the requirements listed above (except for energy-dependent effects which are currently being studied at Los Alamos between 10 and 23 MeV). At 14.5 MeV, two precise elastic measurements are available: $P(\theta)$ for 35 single isotope targets[5] and $d\sigma/d\Omega(\theta)$ from 22 of these in the $A=49$–120 region.[6] With the completion of σ_R measurements on these 22 targets, further optical-model studies[5,6] would appear to be highly beneficial. A particularly striking effect to be investigated in detail is the change in $P(\theta)$ at $\theta=150°$–170° as the target isotopic composition is altered by adding a nucleon.[5]

Further reasons for interest in higher precision σ_R measurements using separated isotope targets are: first, to investigate more carefully the dip in σ_R in the vicinity of nickel; and, second, the conclusion that a surface form factor is necessary at 10 MeV.

Near 10 MeV, σ_R has been measured by beam-attenuation techniques using counters,[7–9] by a beam-attenuation method involving charge integration,[10,11] and by summing partial cross sections.[12–14] The agreement among the various methods is consistent with the experimental accuracy (±5%). Wilkins[15] and Greenlees,[9] in separate analyses, have shown that a surface imaginary potential fits σ_R and $d\sigma/d\Omega(\theta)$ for inter-

* This work was supported by the U. S. Atomic Energy Commission.

† Associated Western Universities-Atomic Energy Commission Graduate Fellow from Texas A. & M. University.

‡ Staff Member from Texas A. & M. University; currently at the University of Maryland.

[1] L. L. Lee, Jr., J. P. Schiffer, B. Zeidman, G. R. Satchler, R. M. Drisko, and R. H. Bassel, Phys. Rev. **136**, B971 (1964).

[2] P. E. Hodgson, in *Proceedings of the International Conference on Nuclear Physics, Paris, 1964* (Editions du Centre National de la Recherche Scientifique, Paris, 1965), Vol. I, p. 257.

[3] M. A. Melkanoff, D. S. Saxon, T. Sawada, and J. S. Nodvik, in *Proceedings of the International Conference on Nuclear Physics, Paris, 1964* (Editions du Centre National de la Recherche Scientifique, Paris, 1965), Vol. II, p. 870.

[4] F. G. Perey, Bull. Am. Phys. Soc. II, **10**, 1205 (1965).

[5] L. Rosen, J. G. Beery, A. S. Goldhaber, and E. H. Auerbach, Ann. Phys. (N. Y.) **34**, 96 (1965).

[6] J. G. Kelly, D. E. Heagerty, H. G. Graetzer, and D. A. Lind, (unpublished).

[7] R. F. Carlson, R. M. Eisberg, R. H. Stokes, and T. H. Short, Nucl. Phys. **36**, 511 (1962).

[8] B. D. Wilkins and G. Igo, Phys. Rev. **129**, 2198 (1963).

[9] G. W. Greenlees, U. Haznedarogen, A. B. Robbins, P. M. Rolph, and J. Rosenblatt, Nucl. Phys. **49**, 496 (1963).

[10] J. Delaunay, B. Delaunay, and J. P. Passerieux, in *Proceedings of the International Conference on Nuclear Physics, Paris, 1964* (Editions du Centre National de la Recherche Scientifique, Paris, 1965), Vol. II, p. 880.

[11] K. Bearpark, W. R. Graham, and G. Jones, Nucl. Phys. **73**, 206 (1965).

[12] N. M. Hintz, Phys. Rev. **106**, 1201 (1957).

[13] R. D. Albert and L. F. Hansen, Phys. Rev. **123**, 1749 (1961).

[14] J. Wing and J. R. Huizenga, Phys. Rev. **128**, 280 (1962).

[15] B. D. Wilkins, thesis, University of California Report No. UCRL-10783, 1963 (unpublished).

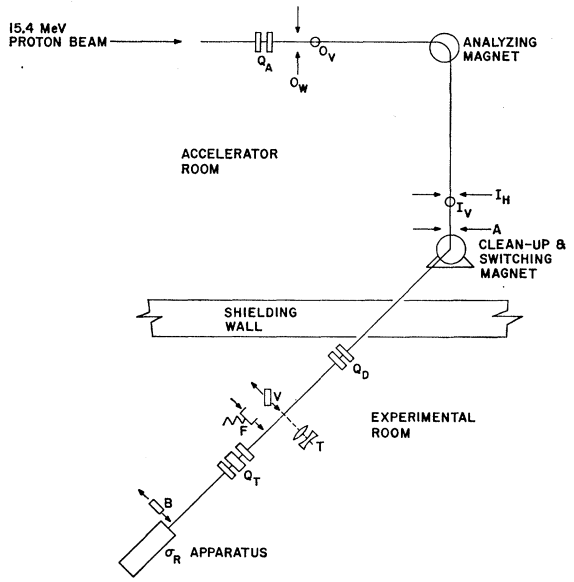

FIG. 1. A diagram of the experimental layout. The symbols have the following meanings: Q_A, Q_D, and Q_T are quadrupole doublets and a triplet, respectively; O_W, O_V, and I_V are horizontal and vertical object slits and the vertical image slit; I_H is the control slit placed at the image position; A is a beam-attenuation slit; V, F, and B are respectively a movable quartz for viewing by remote television, T, a Faraday cup, and a beam stop for beam pictures.

mediate elements better than a volume imaginary potential.

A 10% dip in σ_R in the vicinity of nickel was observed[8] at 10 MeV and has been more recently seen at 28 MeV,[16] at 17 MeV,[17] and near 10 MeV.[10–11] The dip was attributed to a reduction in nuclear size by Igo and Wilkins. This surmise was investigated quantitatively by Wilkins,[15] who analyzed $d\sigma/d\Omega(\theta)$ for 9.85-MeV protons on nickel and 10.2-MeV protons on copper with variable surface-absorption form factors. He obtained σ_R values of 667 and 853 mb in good agreement with measured values of 680±30 and 840±30 mb. The surface absorption form factor was appreciably more sharply peaked for nickel than for copper. Consideration was given to the possibility that the dip could be attributed to the isospin term $(N-Z)/A$ in the real potential[17] or alternatively to the high (p,n) threshold in nickel.[16] However, the former is practically ruled out by the observation of a dip in the 40-MeV alpha-particle σ_R results,[18] and the latter cannot be the entire explanation since the effect persists at higher proton energies[16] and for 40-MeV alpha particles where the (α,n) threshold has little influence. Greenlees[9] and Bearpark[11] observed differences between ^{58}Ni and ^{60}Ni. The data in this paper show that it is possible to understand the presence of this dip for targets having natural isotopic abundances. Measurements of σ_R using separated isotopes increase fairly sharply with increasing neutron number N. This observation, along with the observation that nickel has as its most prevalent isotope an unusually light one, ^{58}Ni, accounts for the observed dip.

II. BEAM-ATTENUATION TECHNIQUE USING COUNTERS

The beam-attenuation technique will be reviewed here briefly. In the present experiment, certain improvements have been incorporated which will be discussed in Sec. III E. In all measurements reported up to now, a beam of protons first passes through two or more passing counters, usually thin plastic scintillation counters, whose outputs activate a coincidence circuit. The scaled output of the coincidence circuit is I_0, the total number of protons involved in the reaction cross-section measurement. A significant number of protons are deflected from the collimated beam by elastic scattering, inelastic scattering, or multiple Coulomb scattering. These are removed from consideration when they strike anticoincident collimator counters which also feed the I_0 coincidence circuit. The emergent beam from the I_0 counter array is incident on the target. Typically, five protons in 10^4 suffer a nonelastic encounter in the target. The attenuated beam of I protons, therefore, differs by a small percentage from I_0. These protons are detected in the stopping counter which subtends a half angle θ_c from the target.

For a target thickness nx where $nx \ll \sigma_R^{-1}$, the reaction cross section is given by the expression

$$\sigma_R = \frac{I_0 - I}{nxI_0} - \frac{i_0 - i}{nxi_0} - \int_{\theta_c}^{\pi} \left(\frac{d\sigma}{d\Omega_{\rm el}}\right) d\Omega + \sigma_{\rm CE} + \eta_3 \frac{n'x'}{nx} + \int_0^{\theta_c} \left(\frac{d\sigma}{d\Omega_{\rm inel}}\right) d\Omega, \quad (1)$$

where n and n' are the target and second-passing-counter atomic densities and x and x' are the target and second-passing-counter thicknesses; i_0 and i are the quantities corresponding to I_0 and I measured when the target is removed; η_3 is defined in Ref. 8.

Interactions in the passing counters or a failure of the anticoincidence-counter discriminators to be fired can contribute to the difference between I_0 and I. The quantities i_0 and i correct for these effects in the second term on the right of Eq. (1). The third term arises from elastic scattering in the target through an angle greater than θ_c. The fourth term is the compound elastic cross section. This term can be important for a light element such as carbon at 10 MeV. At higher energies and for heavier targets, it is expected to be less important and is generally neglected. For instance, the value of $\sigma_{\rm CE}$ for ^{56}Fe is 12 mb at 9.4 MeV and 1.5 mb at 11.7 MeV.[19]

[16] M. Q. Makino, C. N. Waddell, R. M. Eisberg, and J. Hestenes, Phys. Letters **9**, 178 (1964).
[17] R. E. Pollock and G. Schrank, Phys. Rev. **140**, B575 (1965).
[18] G. Igo and B. D. Wilkins, Phys. Rev. **131**, 1251 (1963).
[19] J. Ernst, P. von Brentano, and T. Mayer-Kuckuk, Phys. Letters **19**, 41 (1965).

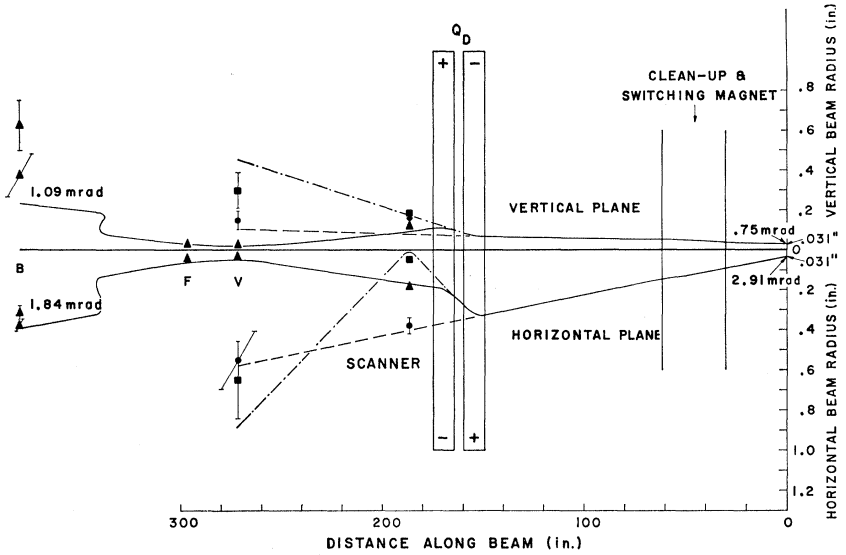

FIG. 2. The results of measurements of the emittance of the beam at I_H. Measurements were made at the automatic beam scanner following Q_D, at V, F, and B (see Fig. 1). The measurements with both elements of Q_D off are indicated by the solid circle and the dashed line; with the first quadrupole of Q_D on, solid square and the dot-dashed line; and with both quadrupoles on, solid triangle and the solid line. The ozalid burner B is located at 485 in. The diagram is not to scale beyond 300 in.

The fifth term is a correction term for scattering out in the second passing counter, which may be as large as 10–20%. This may be particularly important near 10 MeV, in the resonance region near carbon. The sixth term represents inelastic scattering into the stopping counter. In all measurements up to now a sizeable correction represented by the sixth term of Eq. (1) has been required to account for unresolved inelastic scattering since the energy resolution has been poor.

III. EXPERIMENTAL ARRANGEMENT

A. The Proton Beam

Measurements of total reaction cross sections require steady, high-duty cycle beams with good energy resolution and stability. The beam energy should be variable so it can be adjusted to give the desired energy on target without using energy-degrading foils. The Los Alamos Tandem Van de Graaff accelerator used in this experiment meets these requirements. A steady, (15.40±0.01)-MeV beam of protons was produced for an 8-day period spread over 2 wks when the final data were accumulated. The flux from the machine was ordinarily of the order of 0.1 μA, but the beam level was relatively unimportant since the beam was reduced in intensity by many orders of magnitude by the time it reached the apparatus.

B. Experimental Layout

Table I lists the properties of the beam which were obtained by using the beam-handling system of Fig. 1. Proceeding down the beam line (Fig. 1), the beam was first focused to a waist at the horizontal (O_W) and vertical (O_V) object slits by a quadrupole doublet (Q_A). The analyzing magnet focused the beam to a second waist of the same size very near the horizontal control slit (I_H). Then I_H, O_W, and O_V were set to scrape the beam. The fixed-width attenuator slit (A) intercepted the beam envelope as it diverged from the waist at I_H to reduce the beam intensity. The vertical image slit (I_V), variable in width, was adjusted to further reduce the beam. The clean-up and switching magnet bent the beam through 45° and eliminated slit-scattered protons produced at I_H, I_V, and A. The beam size downstream from the attenuation slit (A) as determined from beam-profile measurements was always smaller than the pipe diameter by at least a factor of 4 and well-centered in the pipe to eliminate the possibility of wall scattering. A third waist was located at the position of the pneumatic quartz (V) which could be viewed directly or by television (T). The Faraday cup (F) could be rotated in place to measure the 1 nA beam when the attenuation slit A was in place and I_V was open. Beam spots were taken at the front of the σ_R apparatus at the position of the ozalid burner (B) for final alignment by allowing the beam to impinge on ozalid paper for a short period of time.

C. Beam Optics

In order to obtain the desired beam qualities, it was necessary to measure the emittance of the beam at the control slit I_H. Figure 2 shows the beam at the beam

TABLE I. Properties of the proton beam. (The letters in parentheses refer to Fig. 1.)

Accelerator energy	15.40±0.01 MeV
Energy at the center of the target	14.50±0.15 MeV
Proton flux at the control slit (I_H)	6×10^{11} sec^{-1}
Proton flux at the attenuator slit (A)	5×10^{5} sec^{-1}
Proton flux at the ozalid burner (B)	5×10^{5} sec^{-1}
Size of beam at ozalid burner (B)	0.050 in. (diam)
Horizontal/vertical divergence of beam at ozalid burner (B)	1.8 mrad/1.1 mrad
Horizontal displacement of the beam at ozalid burner (B) for a 50-keV change in beam energy	0.050 in.

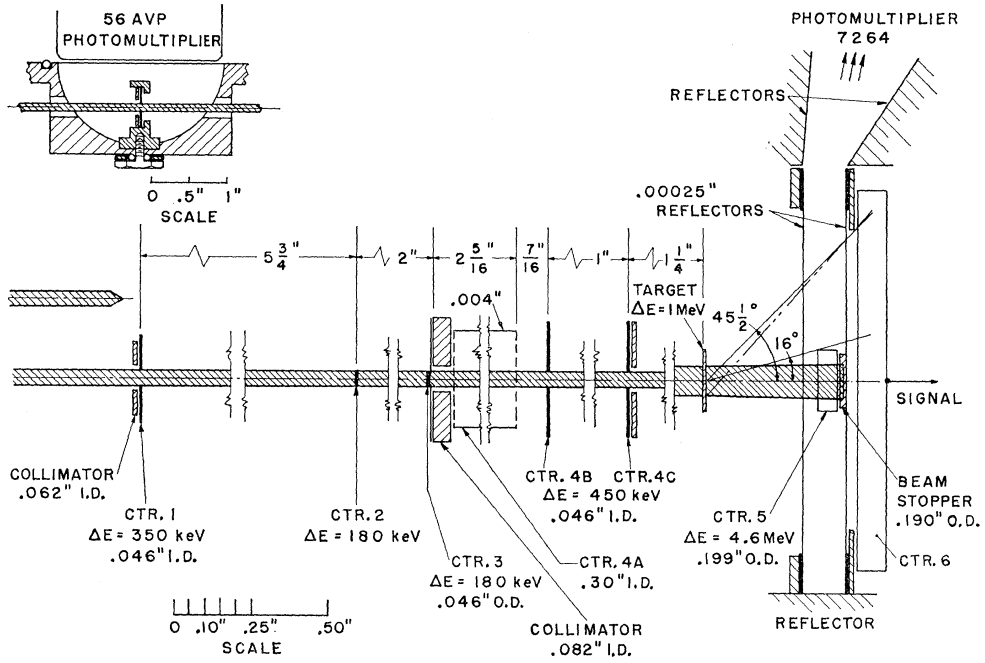

FIG. 3. A schematic diagram of the σ_R apparatus. The arrow at the left shows the shift in beam position associated with a 250-keV energy shift. At the upper left, the configuration of hemispherical reflector, collimator, and plastic scintillator are shown. Counter 4 consisted of three sections, counters 4A, 4B, and 4C. Counter 4A is a tubular collimating counter $2\frac{5}{16}$ in long.

scanners following Q_D, V, and at the position of the Faraday cup F. These profiles were taken with both elements of Q_D turned off, the first element turned on, and with both elements turned on. The currents in the quadrupole elements were set at values calculated in a computer program to produce a waist at V, and then were adjusted slightly to produce a minimum spot size at the pneumatic quartz V. The divergence of the beam at I_H was found to be 0.75 mrad vertically and 2.9 mrad horizontally (spot size 0.06-in. diam). Starting with these values as source emittance parameters, it was possible to calculate the optimum current in Q_T to produce a nearly parallel beam and minimum spot size at the position of the apparatus. The divergence was required to be smaller than the angle determined by the first and last collimator counter in the apparatus (10 mrad vertically and horizontally) and the spot size at the ozalid burner was calculated. The calculation was checked by measuring the spot size (approximately 0.050-in. diam) at the ozalid burner B. When the vertical image slits I_V were closed down to reduce the beam by a factor of 10^4, the vertical emittance was almost certainly further reduced.

D. The σ_R Apparatus

In Sec. II the beam-attenuation method was reviewed. In this section, a description is presented of the method as adapted for this measurement.

It was necessary to maintain the beam-energy resolution by preventing protons from striking metal collimators. The beam, therefore, is defined by a plastic scintillator collimator (collimator counter 1, refer to Fig. 3). The beam's penumbra can strike a slightly larger diameter metal collimator immediately preceding counter 1 placed there to reduce the counting rate. Slit-scattered protons from the metal collimator strike counter 1 and are eliminated by the anticoincidence circuit. The counting rate in counter 1 was low because essentially all beam particles can pass through the 0.046-in. diam hole in counter 1. A smaller scale view of counter 1 is displayed at the upper left to illustrate the method used to collect light from the plastic scintillator. The scintillator and metal collimator are placed in a carefully aligned holder centered in a polished 2-in. diam hemispherical Al reflector. The entrance and exit holes were large enough so that it was impossible to produce a wall-scattered contaminant without two scatterings taking place.

The beam, 0.050-in. diam, deposits 180 keV in each of passing counters 2 and 3. Counter 2 has the highest counting rate of all the counters. Counter 3 is 0.046-in. diam. Only 25% of the protons from 2 strike 3. About 2 protons in 10^4 will backscatter in counter 3. These protons contribute to the target-out factor $(i_0-i)/nxi_0$ (see Sec. II).

Protons scattered from counter 3 in the forward hemisphere strike collimator counter 4. Slit-scattered protons from the metal collimator surrounding counter 3 do not strike it or alternatively strike counter 4, too. Events of the type $(\bar{1}\,2\,3\,\bar{4})$ are I_0 events. A bar indicates an anticoincidence ("no") counter; no bar, a "yes" counter. Because of multiple Coulomb scattering, the profile of I_0 events at the target position is independent of small changes in incident-beam parameters. Unscattered protons pass through counter 5 and into the beam stopper. Protons scattered out to 16° are inter-

cepted by counter 5. A correction is necessary for nonelastic scattering in the forward 16° cone but this is generally of the order of a few mb. Charged particles scattered between 16° and 45.5° deposit energy in counter 6, a lithium-drifted silicon detector. A collimator preceding counter 6 defines an acceptance cone and insures that protons reach the end of range in the sensitive volume even when effects due to finite beam size or possible misalignment of counter 6 are taken into account.

The effect of nuclear absorption in counter 5 when it results in a small deposit of energy is minimal since the discriminator is set to fire even on noise pulses. In earlier measurements,[19] it was set as close to the elastic peak as possible. As a consequence, the ratio of $(I_0-I)/I_0$ to $(i_0-i)/i_0$ is improved from 5:4 to 2.2:1 for medium-weight elements. The energy resolution has been improved to 200 keV by substituting counters 5 and 6 for the stopping counter and by the use of a monochromatic beam ($\Delta E=\pm 10$ keV). The inelastic-scattering correction is reduced to a negligible contribution for most targets. There is no correction necessary in the counter 6 spectrum due to absorption in counter 6 because the undeviated beam particles stop in counter 5. In previous measurements a dummy target was placed in front of the apparatus when the target is out to insure the energy deposited in the stopping counter is the same for target-in and target-out. As a consequence the energy incident on the second passing counter was different. Scattering-out into the backward hemisphere is generally energy-dependent, and therefore a scattering-out correction η_3 as large as 8% was required.[8] The beam profile was also altered by the dummy target. In the present work, no dummy target is required when the target is out. Therefore, no target-out correction arises.

The reaction-cross-section equation (1) reduces to

$$\sigma_R=\frac{I_0-I}{nxI_0}-\frac{i_0-i}{nxi_0}-\int_{\theta_c}^{\pi}\left(\frac{d\sigma}{d\Omega_{c1}}\right)d\Omega+\sigma_{CE} \qquad (2)$$

as a consequence.

IV. ELECTRONICS

A. Electronic Arrangement

The photomultiplier anode signals were used to trigger elements of the fast circuit (see Fig. 4) in which the major part of the pulse sorting was performed. After this initial selection of events, the (I_0-I) events $\bar{1}\,2\,3\,\bar{4}\,\bar{5}$ still contained a significant number of events in which one of the anticoincidence circuits had "failed." Some cases occur in which a proton simply grazes one of the "no" counters and the resulting anode pulse falls below the trigger level of the discriminator. Other cases also occur in which the overshoot from a preceding pulse causes the anticircuit to fail. These erroneous events are removed by use of a fast-slow system (see Fig. 5) designed to examine the dynode outputs of all anticounters for each of the (I_0-I) events.

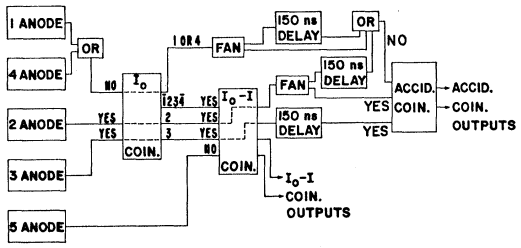

FIG. 4. A schematic diagram of the fast circuit. The I_0-I coincidence circuit outputs and the accidental coincidence circuit outputs are used to trigger elements of the fast-slow circuit depicted in Fig. 5.

The only class of random coincidences that affect the results was that in which a proton was scattered out of the beam in passing counter 2 and at the same time a noise pulse was generated in passing counter 3. A significant number of these random coincidences occurred. Such events depend strongly upon the noise from passing counter 3 during each run, and although such events would cancel if the beam and noise levels were constant, in actual practice both beam and noise levels vary, and, therefore, it is desirable that the number of these events be monitored during each run. This class of random coincidences was measured simultaneously with the real spectrum (see Fig. 4), and the results were displayed in a second 2-dimensional array.

B. Fast Circuit

Figure 4 is a schematic diagram of the fast circuit. Pulses originating at the anodes of counters 1–4 are fed into the I_0 coincidence circuit (1 and 4, "no"; 2 and 3, "yes"). One output of I_0 coincidence circuit is scaled and a second output is fed along with pulses originating at the anodes of counters 2, 3, and 5 into the coincidence circuit measuring I_0-I (2, 3, and I_0, "yes"; 5, "no"). One I_0-I output is scaled.

The random-coincidence circuit illustrated in Fig. 4 performs part of the separation of the class of random events described in Sec. IVA. The principal source of random coincidences which would occur if counter 3 were delayed and no other precautions taken are due to a noise pulse (or a real event occurring later) in passing counter 2. However, when the passing counter 2 pulse was random, no error events would be introduced because a real interaction in counter 3 would be accompanied by a pulse due to a proton in passing counter 2. However, when a proton is scattered out of passing counter 2 and therefore does not strike passing counter 3, an error event can be introduced.

As shown in Fig. 4, a prompt pulse originating at the passing counter 2 anode and a delayed (150 nsec) pulse originating at the passing counter 3 anode are fed into the accidental (Accid.) coincidence circuit in the "yes" mode. The passing-counter-2 pulse is also fed (through an OR circuit with counter 1 and 4 pulses) after 150-nsec delay into the "no" input which will anti-out an event

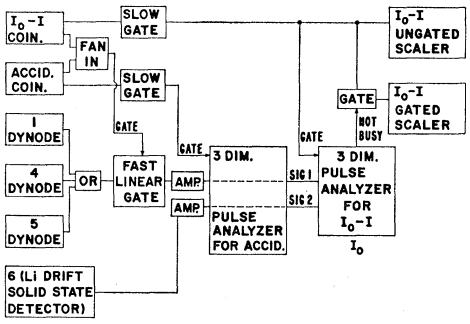

FIG. 5. A schematic diagram of the fast-slow circuit.

when a passing-counter-2 pulse occurs simultaneously with the delayed passing counter 3 pulse at the "yes" inputs of the Accid. coincidence circuit. The 1 or 4 output is fed with prompt timing into the "no" input to remove accidentals in which the pulse from passing counter 3 involved is a random pulse and the proton scattered out of the beam in passing counter 2 goes through the annular gap between passing counter 3 and the metal collimator surrounding counter 3 (see Fig. 3). The 1 or 4 output is also fed with 150-nsec delay into the "no" input to remove another kind of accidental event. If the passing-counting-2 pulse was too small to fire its discriminator and a noise pulse appeared at the "yes" input activated by passing counter 2 simultaneously with a pulse due to a proton at the "yes" input activated by passing counter 3, and additionally the proton scattered into counter 4, the delayed 1 or 4 output would anti-out the event. Outputs from the I_0-I and Accid. coincidence circuits feed a fan-in circuit. The output is used to trigger the linear gates in the fast-slow circuit described in Sec. IVC. Additional outputs from the I_0-I and Accid. coincidence circuits are used to fire the I_0-I (reals) 2-dimensional analyzer and the Accid. 2-dimensional analyzer, respectively.

C. Fast-Slow Circuit

Dynode-derived pulses from counters 1, 4, and 5 are allowed to pass through linear gates each time the fan-in circuit is fired (see Fig. 5). The linear-gate outputs are stretched to 2 μsec and amplified. The outputs of the linear amplifiers pass through an OR circuit. The OR output is fed to one side of each of the 2-dimensional analyzers. Counter-6 pulses, after suitable amplification and delay, are fed into the other side of each 2-dimensional analyzer. The I_0-I and the Accid. coincidence output pulses discussed at the end of Sec. IVB, after suitable lengthening and delay, trigger the I_0-I and Accid. 2-dimensional analyzers, respectively.

In order to displace the spectra away from channel zero on either axis, the linear-gate pedestals are adjusted so a pedestal pulse appears on the output whenever it is gated on by the fan-in output signal with no dynode-derived signal appearing at the inputs. A small fraction of the stretched fan-in derived gate is mixed with counter 6 at the input to displace the spectra in the counter 6 direction. In the display one sees pulses which are that part of the 2-dimensional array where the pedestal pulse, only, appears on the OR circuit input (activated by collimator counters 1, 4, and stopper counter 5). In Sec. VI, which deals with the data reductions, the method used to separate out these events from the I_0-I 2-dimensional arrays will be discussed.

In the Accid. 2-dimensional array, the pulse distribution of interest is that part associated with no pulses appearing in counter 6.

In the OR direction, the events of interest fall into the peak which is called the "miss peak." A small number of miss peak events will arise because of a random coincidence in which both 2 and 3 pulses are noise-induced. It is clear that they give rise to error events and are automatically included in the miss peak. The accidental coincidence circuit was not operative until about half-way through the running period. Fortunately, the beam level was very constant during the entire running period. From the latter half of the data, it was possible to obtain, with good statistical accuracy, the average accidental correction which was applied to the first half as an additional source of error (amounting to $\pm 1.6\%$).

D. Detailed Discussion of Pulse Handling

In this section, the circuit elements in a fast-circuit "yes" arm and a fast-circuit "no" are presented.

1. "No" Arm

Pulses from collimator counter 1 are clipped at the anode by a 5-nsec shorted line and the discriminator fires on the cross-over point to eliminate some of the jitter associated with the large dynamic range of pulse heights (see Fig. 6). A proton passing through the full thickness of the plastic scintillator will deposit 350 keV. Thus, the dynamic range of pulse heights reaching down to a grazing collision is minimized. The "no" counter voltages were adjusted as high as was compatible with the photomultiplier tube's specification, or to a voltage where the pulse due to an average beam proton striking the counter just barely failed to multiple fire the discriminator. The latter limitation arises because of numerous but relatively small after-pulses on the tail of the output pulse lasting for about 100 nsec. The gain must be adjusted so that the afterpulses are below the discriminator level, 125 mV. After suitable delay, the pulse is passed through a 6-dB attenuator to reduce reflected pulse amplitude below 100 mV. The pulse is then amplified by a factor between 5 and 10, inverted to fire on the cross-over, and fed into a fast discriminator (recovery time 10 nsec). Five nsec jitter is introduced by the spectral behavior of the discriminator, and further jitter (3 nsec) is associated with a time-of-flight effect in counter 4. The passing counter

discriminators are another source of 5-nsec jitter. The combined effect of the jitter, transit time spread in the photomultipliers, and required overlap of the passing-counter pulse widths (8 nsec) determine the minimum "no" pulse length. To insure a large safety margin, the "no" pulses were made effectively 40-nsec long. The actual length was 60 nsec, but the trailing 20 nsec of the pulse served another function outlined below.

It was required that no dead time exist during which a "no" pulse would fail to reject an undesired event. To eliminate dead time, the 100-Mc/sec discriminator output was fed to a 50-Mc/sec OR circuit fired also by collimator counter 4. The output was first doubled to 20 nsec by a 10-nsec unshorted clip line, then used to fire a fan-out. Two outputs were delayed 20 and 40 nsec with respect to a third output and the three were mixed in a resistive OR after passing through 6-dB attenuators to reduce the size of reflected pulses arising from imperfect impedance matching. The output pulse, now 60-nsec long, will always have 40-nsec effective "no" pulse width independent of the time interval between successive pulses.

The 60-nsec pulse was amplified to 2 V height whereas a nominal value of 300 mV suffices to anti-out an event. There was a non-negligible over-shoot ($\approx$500 mV high and 200 nsec long) on the "no" pulse when it enters I_0. Closely spaced pulses ($\approx$100-nsec spacing) will diminish the effective height of the last pulse until it will sometimes fail to anti-out the event. In Sec. IVC the fast-slow circuit is discussed which is designed to eliminate these events.

2. "Yes" Arm

The passing-counter-3 arm is shown schematically in Fig. 6. The anode pulse is treated in essentially the same way as a "no" pulse (discussed in Sec. IV D1) until it has passed through the fast discriminator. The output is clipped with a shorted 5-nsec cable to improve coincidence resolution and then fed into a "yes" input of I_0. Passing-counter-3 discriminator is set to 10 Mc so that it will be dead for about 75 nsec. This serves to remove the second of two closely spaced events from the beam which removes some of the events where overshoot causes the "no" pulse to fail (see Sec. IV D1).

E. Counting Rates

The I_0 counting rate in the present experiment was 5×10^3 sec^{-1}, which appears modest considering the fact that nanosecond circuitry is being used. This rate is a factor of 10 less than the average rate of Igo and Wilkins,[8] and when the 50% duty cycle (macroscopic) of the beam used by Igo and Wilkins is remembered, the rate is effectively reduced by a factor of 20. The considerations which set the I_0 rate, however, are the same in both experiments. The counting rate of the individual counters are the limiting factor. The highest counting rate in the individual counters in the two experiments were the same, about 2×10^5 sec^{-1}. In the present experiment, the losses due to multiple Coulomb scattering were much more severe because the beam size was reduced from 0.20 to 0.05 in. in order to reduce the finite beam-size corrections.

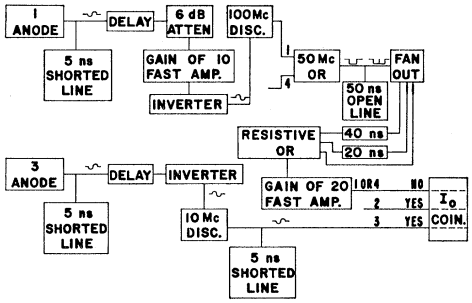

FIG. 6. Fast circuit elements of a "yes" arm and of a "no" arm.

Total reaction cross sections were measured versus counting rate (from I_0 rates of 2500 sec^{-1} to 7500 sec^{-1}) with no change in the size of the measured reaction cross sections.

V. EXPERIMENTAL PROCEDURE

A. Beam Alignment by Counters

The nonelectronic procedure to align the beam up to the ozalid burner, B (see Fig. 1), has already been described in Sec. III. After the beam has been centered well enough so that some of the protons will pass through collimator counter 1, the vertical slit I_V is closed down until it is nearly shut. The vertical slits are opened a little at a time until I_0 counts are observed. The output of the I_0 scaler discriminator is fed into a count rate meter which gives both a visual and audible output to aid the accelerator operator in optimizing the beam by adjusting machine and beam-handling equipment parameters. After optimizing all parameters including the vertical slit I_V width, a steady beam of 5000 sec^{-1} is obtained.

At this point it is possible to check the alignment of the apparatus on the beam line electronically by minimizing the ratio of the (1 2 3 4) rate to the (2 3 5) rate.

B. Measurement of Total Reaction Cross Sections

It was not necessary to run anticoincidence delay curves as a function of counters 1, 4, and 5 delay as a regular procedure because the "no" pulses had an effective length of 40 nsec whereas the overlap necessary was of the order of 20 nsec. The relative timing of the "yes" and "no" pulses was adjusted so "yes" pulses fell approximately 15 nsec after the beginning of the "no" pulses. Routine voltage checks and pulse-height checks were made to assure that the outputs did not vary. Discriminator outputs were viewed to assure that multiple firing due to after-pulsing was absent (see Sec. IV D1). Routine timing checks were made during

TABLE II. Target thickness measurements used in obtaining σ_R. The areal density was obtained by punching out that area of the target which was bombarded by the beam. The quantity nx is the number of atoms per cm² obtained from the areal density; $(nx)_T$ is the number of atoms per cm² obtained from the target prior to punching out the portion bombarded by the beam; $(nx)_{\Delta E}$ is the number of atoms per cm² obtained from energy-loss measurements. All (nx) values were corrected for isotopic impurities.

Most abundant isotope	Areal density (mg/cm²)	nx (10^{20} cm^{-2})	$(nx)_T$ (10^{20} cm^{-2})	$(nx)/(nx)_T$	$(nx)_{\Delta E}/nx$
^{49}Ti	42.89	5.278	5.247	1.006	1.06
^{54}Fe	52.79	5.889	5.816	1.013	···
^{56}Fe	52.06	5.615	5.632	0.997	1.06
^{57}Fe	50.15	5.314	5.177	1.026	···
^{58}Fe	50.71	5.272	5.198	1.014	1.07
^{58}Ni	55.69	5.788	5.834	0.992	···
^{60}Ni	46.90	4.715	4.736	0.996	1.04
^{62}Ni	61.03	5.936	5.920	1.003	···
^{63}Cu	55.54	5.315	5.229	1.016	1.05
^{65}Cu	54.02	5.011	5.012	1.000	1.05
^{64}Zn	51.20	4.824	4.759	1.014	1.05
^{66}Zn	48.13	4.397	4.300	1.022	1.03
^{68}Zn	55.29	4.902	4.878	1.005	1.06
^{90}Zr	43.14	2.890	2.883	1.002	1.03
^{91}Zr	60.54	4.011	4.011	1.000	1.06
^{92}Zr	56.88	3.728	3.720	1.002	1.05
^{94}Zr	54.22	3.477	3.480	0.999	1.06
^{116}Sn	55.18	2.868	2.903	0.988	1.08
^{117}Sn	55.81	2.875	2.863	1.004	1.17
^{118}Sn	50.74	2.592	2.536	1.022	1.06
^{119}Sn	51.18	2.592	2.408	1.076	1.04
^{120}Sn	54.38	2.732	2.747	0.994	1.05

the course of the running day to assure that the pulse arrival times into the I_0, I_0-I, and Accid. coincidence circuits and that the pulse arrival times at the linear gates were unchanged from their proper values. The gains of the μsec amplifiers were checked by observing the height of the pedestal pulses. The I_0 output was monitored by two scalers; the (I_0-I) output, the gated (I_0-I) output, and the Accid. coincidence output were monitored by scalers. During target-out runs, the ratio of (I_0-I) and I_0 scalers was 1/1500; during target-in runs, between 1/350 and 1/500 depending on whether the target was a high-Z or low-Z target. The ratio of the Accid. scalers output to the (I_0-I) scalers output was 1/4 with target-in and 1.5/1 with target out. The latter ratio exceeds unity because only a fraction of the Accid. scaler pulses were significant (see Sec. IV C). The (I_0-I) 2-dimensional pulse distribution was concentrated in the miss peak with the target out. With the target in, about 40% of the pulses fell in the miss peak and about 60% in the elastic peak. The beam level and stability were constantly monitored by the operator. Target-out runs of 1.25×10^7 I_0 events were interspersed between groups of 4 to 6 target-in runs of 2.5×10^7 I_0 events.

C. Beam Profile at the Target

The beam profile at the target is essentially independent of the beam characteristics at B (see Fig. 1). The beam characteristics at B may change from time to time during the run because of retuning of the accelerator, i.e., small changes in the beam direction and changes in the beam-distribution profile may occur. The independence from beam characteristics is due to multiple Coulomb scattering in passing counters 2 and 3 where 90% of the beam protons are scattered out of the beam. The residual 10% of the beam which is incident on the target is the distribution at the center of the product of two folded Gaussian distributions whose individual angular widths are larger than the angular width of the beam defined by the collimator counters and passing counter 3. The beam profile at the target was quite uniform, decreasing by only 30% from the center to edge of the target area bombarded by the beam. In order to obtain this result, a computer program was developed to follow a statistically significant sample of beam protons through the plastic scintillators, introducing distributions appropriate for the multiple Coulomb scattering process occurring there.

D. Target-Thickness Measurements

The areal density of the target foils was determined by weighing the target foils and determining their areas (about ten times the beam size) before the measurements were performed. After the measurements were completed, the area actually bombarded by protons, 0.12 in. in diameter, was punched out and weighed. The precision of the punch was indicated by the fact that the fluctuation in radius from target to target was less than 0.6%. The results are summarized in Table II. The diameter of each target was measured to at least an accuracy of $\pm0.2\%$. The edges of the targets were examined for roughness, and small corrections to the areas (always less than $\pm0.1\%$) were made if necessary.

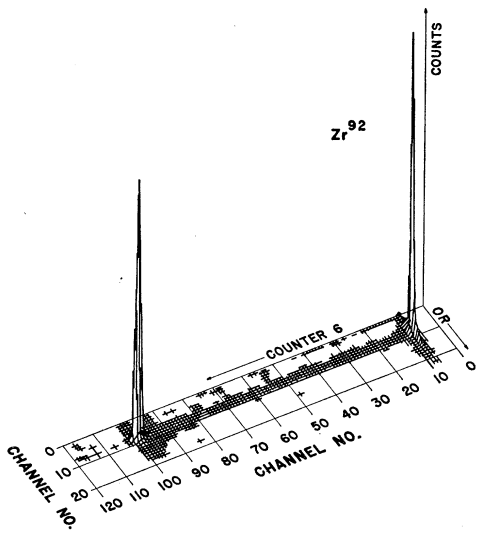

FIG. 7. A 2-dimensional display of the data obtained for a typical target-in run.

The weight uncertainty is less than $\pm 0.4\%$. Therefore, the uncertainty introduced into the measurement of σ_R is less than or equal to $\pm 1\%$. The next to the last column in Table II lists the ratio of the areal densities. The ratio in all but one case differs from unity by the order of 1% or less, indicating that the targets are uniform since the areas differed by a factor of 10. When it is recalled that Coulomb scattering in counters 2 and 3 diffuses the beam producing a uniform illumination of the target over an area 0.120 in. in diameter, the error due to nonuniformity in target thickness is not expected to introduce further uncertainty in the results.

A possible source of error which has not been considered in the error evaluation could arise from channeling in the polycrystalline targets. This would allow some incident protons to see fewer target nuclei than would be expected on a purely statistical basis with a given number of nuclei per cm^2.

In addition to determining (nx) values by the method described above, the quantity $(nx)_{\Delta E}$ was determined by energy-loss measurements. The beam energy was reduced to 9 MeV and counter 5 was removed. Counter 6 was moved back to intercept a 13° solid angle to reduce kinematical energy spread. The energy deposited in counter 6 was measured with the target in and out. The energy loss $dE/d\rho$ was calculated using the ionization potentials of Bischel[20] and integrated to determine the thickness of the target. The ratio of $(nx)_{\Delta E}/(nx)$ is listed in Table II. The average value of the ratio is fairly consistent but exceeds unity by approximately 6%, which may be due to a nonlinearity in the electronic pulse-height response function. The (nx) values obtained by punching out a foil the size of the beam were used in further analyses to obtain the reaction cross section.

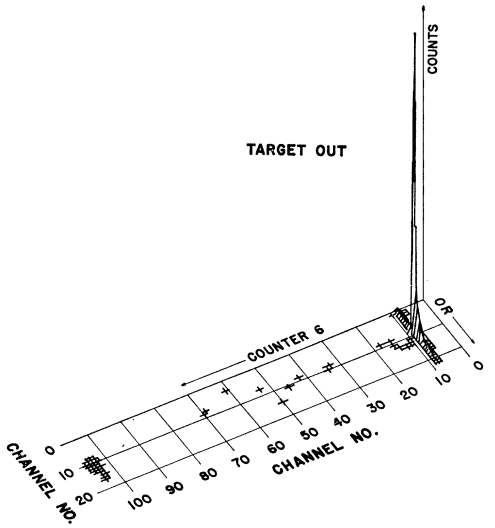

FIG. 8. A 2-dimensional display of the data obtained for a typical target-out run.

[20] H. Bischsel (private communication).

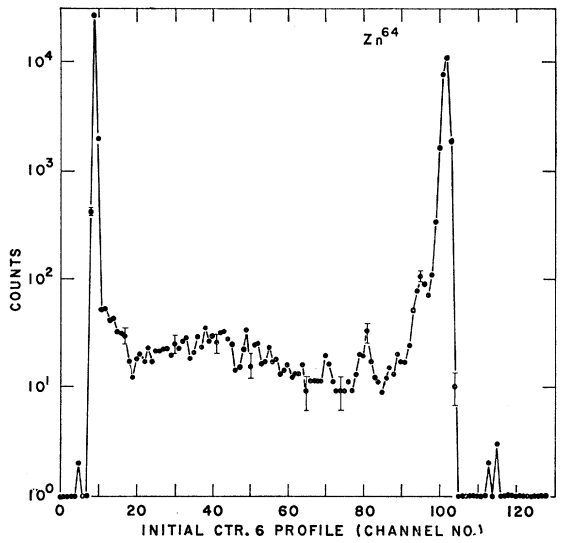

FIG. 9. Counter 6 spectrum summed in the OR direction for ^{64}Zn target. The solid straight lines connect neighboring points.

VI. DATA REDUCTION

The 2-dimensional analyzer data is read out initially onto paper tape and later analyzed with the help of a fast computer. Sample data for target-in and target-out runs are displayed in Figs. 7 and 8. The pulse amplitude in counter 6 is recorded versus the OR output (sum of dynode outputs for anticoincidence counters 1, 4, and 5). The desired events occur principally in channels 7, 8, and 9 in the OR direction while some erroneous events (accompanied by pulses in the 1, 4, or 5 counters) are evident. The procedures followed in separating these data into component parts are outlined below.

A. Separation of OR Events for Target-In Runs

The data for a target-in run were first summed in the OR direction. Figure 9 shows the spectrum that results, plotted in the counter 6 direction. The miss peak appears in channel 9, the elastic peak in channel $101\frac{3}{4}$, and inelastic scattering to the first few excited states is clearly discernible. The spectrum contains some events in which one of the collimator counters has been struck. Because of noise, the miss peak has a finite width in both the counter 6 and OR directions. The problem discussed in this section is to determine the miss-peak profile in the OR direction after elimination of OR events. Data near the elastic peak are used as a source of the miss peak profile free of OR contamination.

If the collimator counter is struck, the energy of the proton striking counter 6 will be reduced, and the event will tend to fall on the lower side of the counter-6 elastic peak. Furthermore, the probability that a slit-scattering proton in a collimator counter will elastically scatter from the target into counter 6 is relatively small. Events where a proton grazes stopping counter 5

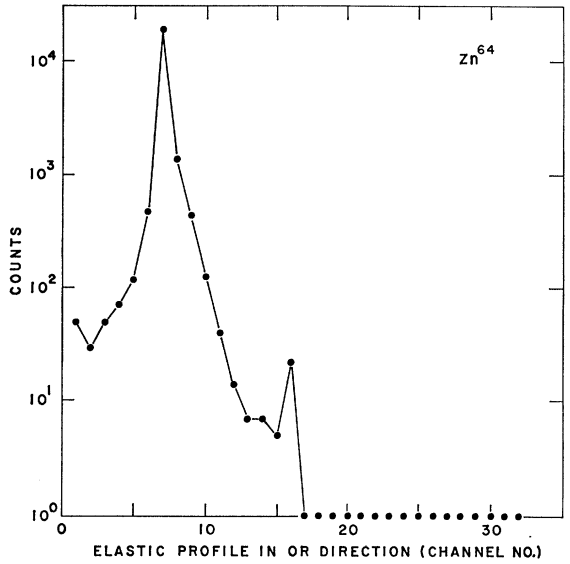

FIG. 10. Elastic peak spectrum versus OR channel summed between channel 100 and channel 103 of counter 6 for ^{64}Zn. The solid straight lines connect neighboring points.

and passes into counter 6 are more probable, but these will again tend to fall on the lower side of the counter 6 elastic peak. Consequently, the elastic-peak form factor in the OR direction is free of events where the collimator or stopping counters have been struck, provided the channels on the lower side are excluded. An upper and lower channel in the counter-6 direction are chosen to bracket the elastic peak (see Fig. 9). The computer then sums in the counter-6 direction between the given channels and displays the resulting spectrum in the OR direction (Fig. 10). The spectrum in Fig. 10 contains some events in channels above the peak which are clearly not associated with the peak shape. An elastic-peak profile is fed back into the computer, differing from Fig. 8 in this respect. Figure 11 shows the profile chosen as well as the data points of Fig. 10.

This "proper" profile for the miss peak in the OR direction can now be used to reject those events where a small pulse was present in counters 1, 4, or 5. The elastic peak profile is next normalized to the sum of counts below and including the peak channel of the miss peak excluding channel 1. The result is shown in Fig. 12. Events on the high side of the peak are associated with unwanted OR events and can be eliminated in a straightforward manner. A group of pulses near zero channel which decrease exponentially with channel number are also eliminated. These events are due to the negative overshoot of a pulse which occurred shortly before the linear gate opened, where the corresponding overshoot in the fast coincidence has caused the anticoincidence circuit to fail. Clearly these pulses should not be included in the miss peak since they are not true (I_0-I) events.

Summarizing, the separation of unwanted events where OR counters have been struck is accomplished by fitting the elastic-peak profile to the miss-peak data as described above. The low side of the miss-peak profile is summed, after elimination of a group in channel 1, and added to the counts in the high side of the miss peak obtained from fitting the elastic-peak profile. The removal of OR counts in the central region of counter 6 direction is accomplished by averaging the "acceptance fractions" used for the elastic-peak and miss-peak regions of the data. Having removed the events containing an interaction with one of the OR counters, the

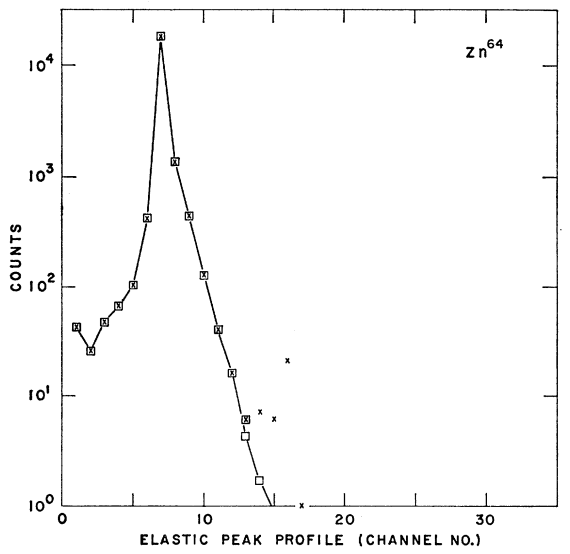

FIG. 11. The elastic peak profile and the elastic peak spectrum.

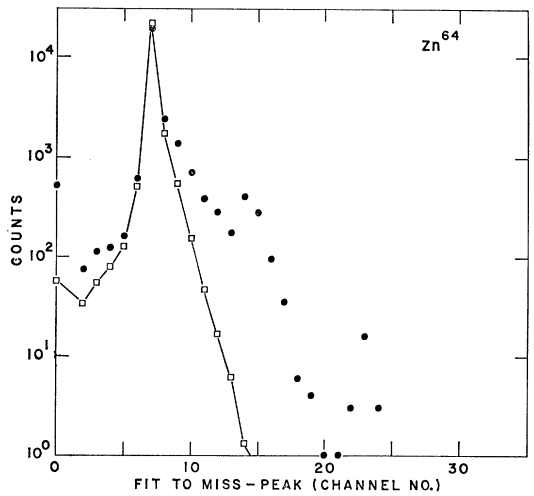

FIG. 12. Miss-peak spectrum versus OR channel for ^{64}Zn summed between channel 1 and channel 15 of counter 6 is denoted by solid circle. The points, open squares, which are connected by solid straight lines, are the normalized elastic peak profile.

computer presents a new counter 6 spectrum as shown in Fig. 13.

B. Separation of Elastic Events for Target-In Runs

The energy resolution of counter 6 is 200 keV full width at half-maximum, (FWHM) for elastically scattered protons from Au. Kinematic effects broaden the elastic peak for the lighter targets. For many of the even isotopes under investigation the first-excited states are separated by an amount in excess of 1 MeV from the ground state. The elastic-peak shape for these isotopes was similar to that observed for gold, but differed in width as discussed above. From a study of these shapes after the removal of the inelastic contribution in a consistent fashion, it was possible to obtain shapes for the low-energy side of the spectrum which could be applied to the odd-A targets, where the first-excited states are not clearly resolved (see Fig. 14). Therefore, the separation of the elastic events can be performed with some confidence except in the case of some odd-A nuclei with states lying at energies considerably less than 200 keV. The computer presented a remainder spectrum obtained by subtracting off the elastic events and summed the counts in the remainder spectrum (see Fig. 15).

C. Separation of OR Events for Target-Out Runs

The analysis of target-out runs was the same as the target-in runs except that no elastic-scattering events appear in the counter-6 spectra. Figure 16 shows a typical target-out spectrum in the counter 6 direction after summing in the OR direction. It is desirable to use the same procedure for eliminating OR events described in Sec. VI A. An elastic-peak profile was obtained from the target-in runs immediately before and after the target-out run. Otherwise the procedure was the same as outlined in Sec. VI A to obtain the remainder runs. In most cases, the remainder sums obtained using target-in runs before and after the target-out did not differ significantly and were averaged to obtain the value used in the subsequent analysis.

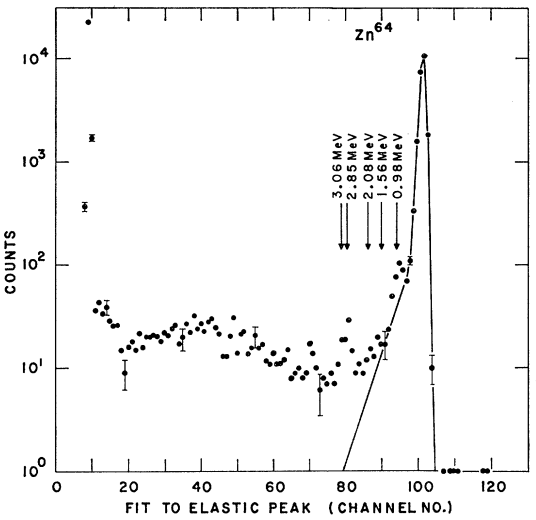

FIG. 14. Separation of the elastic peak from the counter 6 spectrum for ^{64}Zn. The straight solid lines connect points in the elastic peak spectrum. The arrows show the positions of low-lying states in ^{64}Zn.

D. Elastic-Scattering Correction

The elastic-scattering term in Eq. (2) was calculated using 14.5-MeV data[6] which has an uncertainty of 4% on the absolute cross section and additional uncertainty

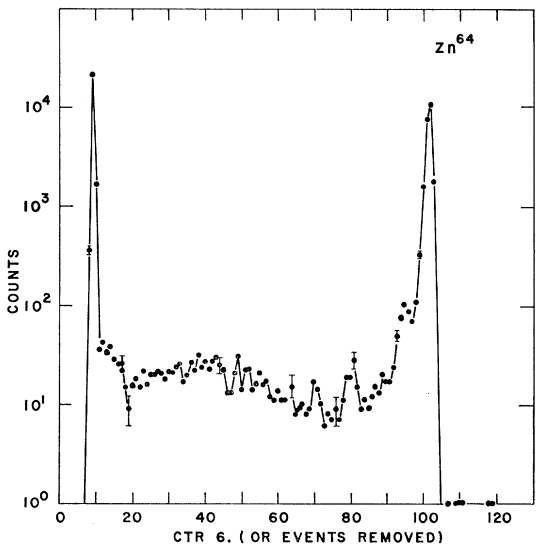

FIG. 13. Spectrum of counter 6 summed over the OR channels with events eliminated where there was a pulse in counters 1, 4, or 5.

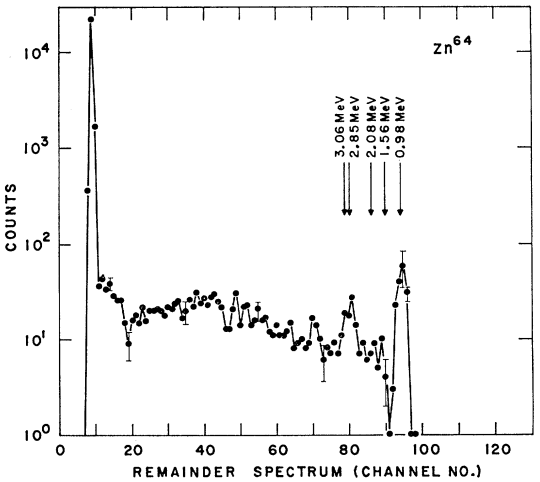

FIG. 15. The spectrum in counter 6 remaining after the removal of the elastically scattered events for ^{64}Zn.

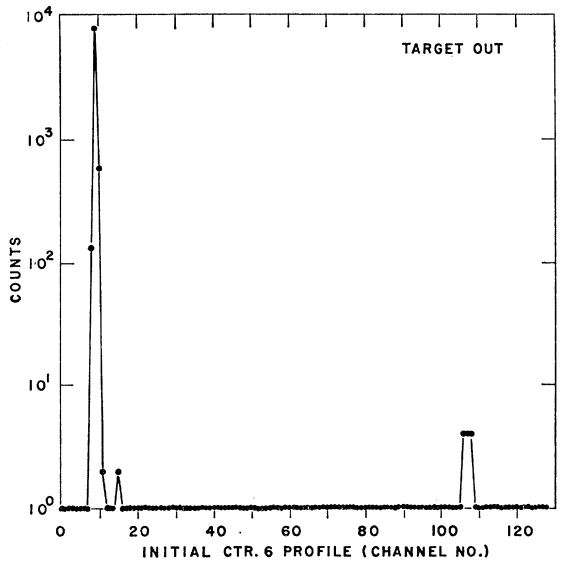

FIG. 16. A typical target-out spectrum summed in the OR direction.

on the relative values. Counter 6 subtended a large enough angle, approximately $45\frac{1}{2}°$, so that the elastic-scattering correction contributed an uncertainty to σ_R of only approximately 1% for the lighter isotopes and about 3% for the Sn isotopes.

The elastic-scattering correction was calculated taking into account the finite size of the beam and the angular distribution of multiple Coulomb scattering in the passing counters and in the target. Figure 17 illustrates the weighting function which results from these effects. It was obtained by following a distribution of particle trajectories through the counters and the targets, weighting each trajectory according to the multiple Coulomb-scattering distribution and then investigating the scattering at the target for each trajectory using the elastic-scattering data from Ref. 6. Table III lists the elastic-scattering correction for each target.

E. Correction for Random Coincidences

The method for obtaining random coincident I_0-I events is discussed in Sec. IVB. Since the first 50% of the data was taken before the random-coincidence circuiting was set up, an additional source of error of $\pm 1.6\%$ was added quadratically to the error estimate for the first 50% of the data. This source of error was worked out by calculating the expected random-coincidence correction from the last 50% of the data. There was no correction to the reaction cross section because the random counts cancelled out on the average in the subtraction of target-out runs from target-in runs.

F. Measurement of a Counter-5 Dead-Layer Effect Between Target-In and Target-Out Runs

A possible source of error on the absolute value of the reaction cross section (but not on their relative values) might arise because the proton energy incident on counter 5 differed by 1 MeV with the target in and out. The target-out measurements were made without a dummy target. This has the advantage that the beam distribution is not altered and the energy incident on the plastic scintillators is not changed. However, the energy incident on counter 5 changes by 1 MeV when the target is taken out. Although we raised the counter 5 voltage as high as the tube characteristics would allow and used the fast-slow circuit to exclude even smaller pulses which do not fire the discriminator, there was a small but finite "dead" layer on the front surface of counter 5. This is a region where an incident particle may go undetected if a nuclear interaction occurs which produces only uncharged decay products, because the energy lost in the plastic scintillator when converted to light was insufficient to be detected. We believe this layer to have a negligible effect, but as a check we have measured the reaction cross section for a 1-MeV thick graphite target at 14 and 15 MeV. Any difference between the measured values may be due to difference in σ_R in the target material or in the front layer of counter 5 as well.

Table IV lists the results of the measurements at 14 MeV and 15 MeV incident on counter 5. The values of $nx\sigma$ differ by 0.6%, which is an amount which is less than the experimental error on each measurement. From this measurement, it can be concluded that even if the "dead" layer on the front surface of counter 5 were of appreciable thickness, the results would not be in error because of the energy difference incident on counter 5.

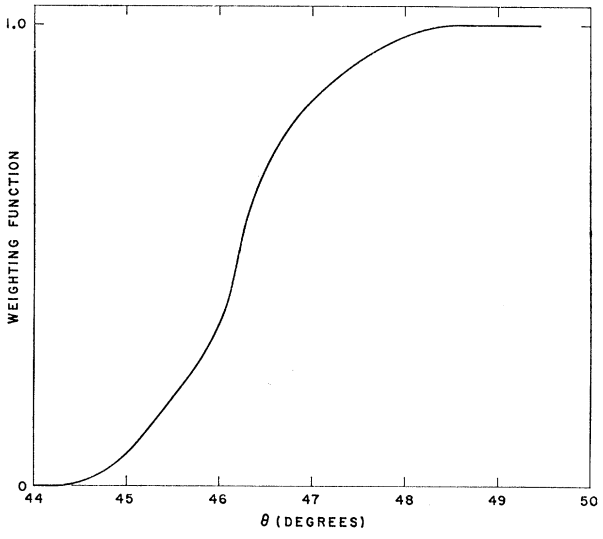

FIG. 17. The weighting function for the elastic-scattering correction.

TABLE III. Total reaction cross sections and quantities used in calculations. All terms are defined in the text.

Most abundant isotope	nx (10^{20} cm^{-2})	I_0 (10^6)	I_0-I	i_0 (10^6)	i_0-i	$\int_{\theta_c}^{\pi}\left(\frac{d\sigma}{d\Omega_{el}}\right)d\Omega$ (mb)	σ_R (mb)	$(\sigma_R)_{av}$ (mb)	$(\sigma_R)_{corr}$ (mb)
^{49}Ti	5.278	25.132	27272	12.270	6190	172	928±27	931±19	931±19
		25.243	30531	14.669	9168		935±28		
^{54}Fe	5.889	24.914	27625	26.639	12663	198	878±21	869±16	865±16
		25.477	28717	25.201	12764		856±25		
^{56}Fe	5.615	24.973	29425	12.270	6190	177	1023±28	1003±19	1012±19
		25.012	28022	12.533	5868		984±27		
^{57}Fe	5.314	25.446	27147	26.639	12663	161	952±21	979±14	976±14
		25.517	29084	12.270	6190		1034±28		
		23.946	28181	17.094	9556		1002±28		
^{58}Fe	5.272	25.224	29216	12.270	6190	152	1088±29	1057±20	1069±20
		28.240	33384	17.094	9556		1030±27		
^{58}Ni	5.788	25.217	29380	25.201	12764	211	927±27	927±27	927±27
^{60}Ni	4.715	25.016	25385	26.639	12663	187	957±24	978±16	978±16
		25.132	26642	12.270	6190		991±30		
		25.742	26906	25.464	12442		994±28		
^{62}Ni	5.936	26.330	32308	12.270	6190	178	1039±29	1066±20	1067±20
		25.011	32643	20.818	11492		1091±28		
^{63}Cu	5.315	25.057	27116	14.556	6744	178	986±24	985±18	985±18
		25.195	28316	25.201	12764		984±27		
^{65}Cu	5.011	25.337	26868	26.639	12663	173	994±22	1000±14	1000±14
		25.592	27444	27.117	12933		1015±23		
		27.786	30084	22.777	11391		990±27		
^{64}Zn	4.824	25.011	25506	14.556	6744	198	956±25	965±16	965±16
		26.350	27931	25.464	12442		986±28		
		24.998	27653	25.083	13786		956±28		
^{66}Zn	4.397	25.023	24829	14.556	6744	184	1019±26	1035±19	1036±19
		25.021	26310	25.201	12764		1056±29		
^{68}Zn	4.902	25.057	27032	26.684	12418	177	1074±23	1074±17	1075±17
		25.197	27484	27.177	12933		1075±24		
^{90}Zr	2.890	25.038	20123	27.254	12419	300	904±34	904±34	902±34
^{91}Zr	4.011	25.534	24347	27.254	12419	309	932±30	932±30	929±30
^{92}Zr	3.728	25.023	23445	27.254	12419	292	999±30	1008±23	1011±23
		25.010	24971	12.931	6574		1022±36		
^{94}Zr	3.477	25.304	23765	27.254	12419	318	1073±32	1087±24	1093±24
		25.040	25089	25.201	12764		1107±37		
^{116}Sn	2.868	26.266	24606	26.684	12418	530	1114±45	1114±45	1113±45
^{117}Sn	2.875	25.116	23851	13.986	6743	514	1112±47	1112±47	1107±47
^{118}Sn	2.592	25.274	23422	13.986	6743	518	1197±50	1192±29	1194±29
		25.005	25091	17.094	9556		1197±52		
		26.962	26864	37.768	21354		1184±49		
^{119}Sn	2.592	25.181	22923	13.986	6743	538	1114±50	1114±50	1109±50
^{120}Sn	2.732	25.149	23592	13.986	6743	520	1149±48	1150±34	1152±34
		26.787	24632	14.556	6744		1150±48		

G. Total Reaction Cross Sections—Results

Table III lists the reaction cross sections obtained for each run and the experimental quantities that enter into the calculation of σ_R in Eq. (2). In the cases where there were several values $(\sigma_R)_i \pm (\delta\sigma_R)_i$ for one isotope, an average value $(\sigma_R)_{av} \pm (\delta\sigma_R)_{av}$ has been obtained by calculating the quantity

$$(\sigma_R)_{av} \pm (\delta\sigma_R)_{av} = \frac{\sum_i [(\sigma_R)_i/(\delta\sigma_R)_i^2]}{\sum_i [1/(\delta\sigma_R)_i^2]} \pm \frac{1}{\sum_i [1/(\delta\sigma_R)_i^2]}. \quad (3)$$

The last column in Table III lists $(\sigma_R)_{corr}$ which is the value of $(\sigma_R)_{av}$ corrected for isotope impurities in the targets.

The energy at the centers of the targets was approxi-

TABLE IV. Attenuation measurements for protons incident on graphite.

Energy incident on counter 2 (MeV)	I_0 (10^6)	I_0-I	i_0 (10^6)	i_0-i	$\frac{(I_0-I)}{I_0}-\frac{(i_0-i)}{i_0}$ (10^3)
15.4	25.288	39504	12.653	5920	1.0943
16.4	25.071	37861	13.692	5784	1.0877

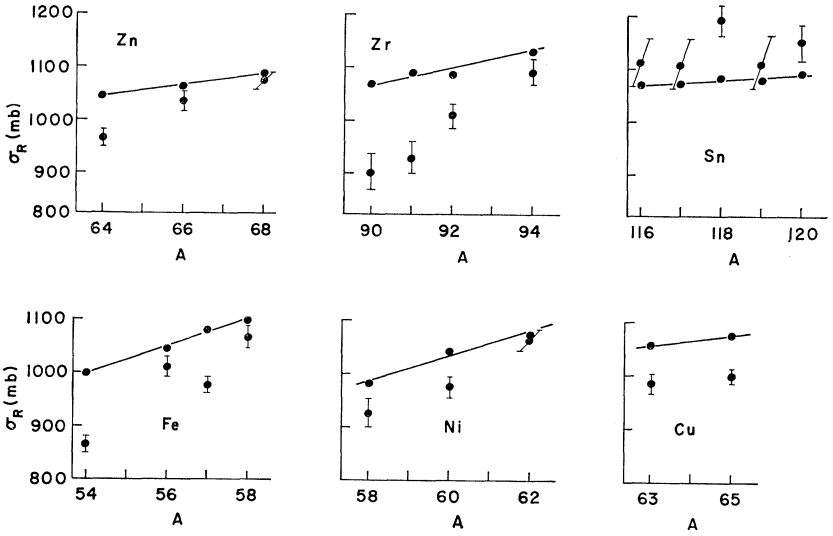

FIG. 18. The total reaction cross sections as a function of atomic mass. The points without error bars are the values obtained from optical-model calculations. The points with error bars represent the values obtained from this experiment.

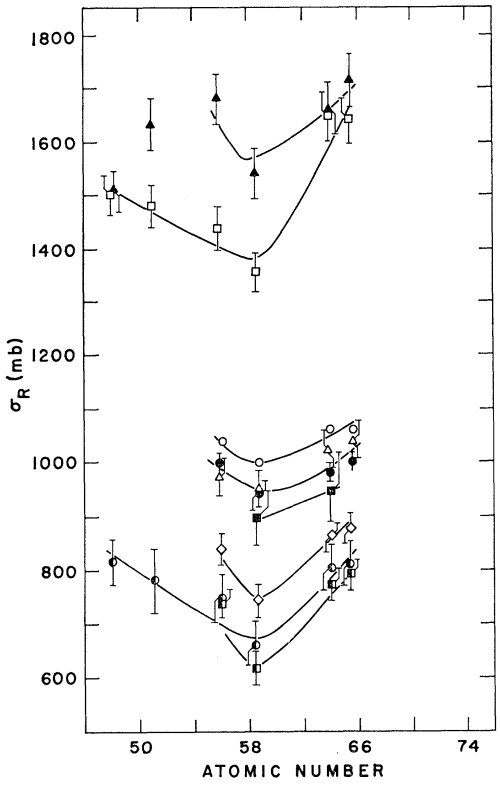

FIG. 19. The nonelastic cross section σ_R-σ_{CE} versus atomic mass. The curves join points from the same experiment. The solid triangles are for 26.5-MeV deuterons (Ref. 23); open squares for 40-MeV α particles (Ref. 18); open triangles for 28-MeV protons (Ref. 16); solid square for 16-MeV protons (Ref. 17); open diamond for 11.5-MeV protons (Ref. 11); half closed circle for 10-MeV protons (Ref. 8); and half closed square for 9.75-MeV protons (Ref. 11). The closed circles are obtained by weighting the measured values in this experiment. The open circles are obtained in the same way using the optical-model values of σ_R from Ref. 3.

mately 14.5 MeV. Since energy-loss measurement in the targets reported in Sec. VD were consistently a few percent high compared with values quoted in the literature,[20,21] no attempt was made to obtain the actual energy at the center of the target. The energy incident on counter 2 was 15.40±0.003 MeV, the thickness of counters 2 and 3 were 0.002 in.±0.0001 in., and they were fabricated from ^{102}Ne plastic scintillator.[22]

VII. CONCLUSIONS

Total reaction cross sections σ_R have been measured for 22 isotopically pure targets at 14.5 MeV (see Table III). Good measurements of $P(\theta)$[5] and $d\sigma/d\Omega(\theta)$[6] already exist. The uncertainties which can be quantitatively accounted for amount to approximately ±2% for the lighter elements increasing to approximately ±4½% for the Sn isotopes.

The results may be compared with the optical-model calculations[6] of σ_R utilizing the $P(\theta)$ and $d\sigma/d\Omega(\theta)$ data (the σ_R predictions are very similar when only $P(\theta)$ data are analyzed[5]). The results are compared in Fig. 18 with the optical-model predictions of Ref. 6. It can be seen that the predicted values of σ_R are generally smaller except for Sn, where the experimental values are lower. The most obvious difference is that the measured values of σ_R increase with N for fixed Z more rapidly than do the optical-model predictions for Ni, Fe, Zn, and Zr.

Since 1963 it has been known that σ_R showed a 10% dip in the nickel region when targets of natural isotopic abundance are used.[8,18,16,23,11,17] The effect shows up in

[21] C. Williamson and J. P. Boujot, Commissariat à l'Energie Atomique, CEA-2189, 1962 (unpublished).
[22] Nuclear Enterprises, Ltd., 550 Berry St., Winnipeg, Canada.
[23] S. Mayo, W. Schimmerling, M. J. Sametband, and R. M. Eisberg, Nucl. Phys. **62**, 393 (1965).

the 9–40-MeV region for protons, deuterons, and alpha particles. Figure 19 illustrates the data of Refs. 8, 18, 16, 23, 11, and 17 as well as our data and the optical-model data,[6] where the last two have been averaged over the natural abundances. It then is easy to discern the minimum occurring. This evidence shows that the nickel reaction cross section is small because of the presence of comparatively light ^{58}Ni as the prevalent isotope in nickel which reduces the value of σ_R for the element relative to neighboring elements by about 10%.

ACKNOWLEDGMENTS

We are indebted to the staff of the *P*-9 group for producing a very fine 14.5-MeV proton beam and for providing excellent experimental facilities to help with the preparation of the experiment equipment. A loan of the mechanical parts of the σ_R gear used by Igo and Wilkins by the Lawrence Radiation Laboratory is gratefully acknowledged. We are indebted to L. Rosen for the loan of the isotopically pure targets used in these measurements.

PHYSICAL REVIEW VOLUME 157, NUMBER 4 20 MAY 1967

Search for Members of the Two-Phonon Triplets in ^{80}Se and ^{80}Kr

A. V. RAMAYYA AND J. H. HAMILTON
Vanderbilt University, Nashville, Tennessee*

AND

B. VAN NOOIJEN†
Oak Ridge National Laboratory, Oak Ridge, Tennessee‡ and Vanderbilt University, Nashville, Tennessee

AND

NOAH R. JOHNSON
Oak Ridge National Laboratory,‡ Oak Ridge, Tennessee

(Received 8 December 1966)

The γ rays emitted in the decay of ^{80}Br have been investigated with Ge(Li) and NaI(Tl) spectrometers. γ rays (relative intensities are in parentheses) of 616.2±0.5(100), 639.2±0.7(3.6), 665.6±0.5(17.2), 704.0±0.7(2.9), 812.0±1.5(0.8), and 1256.4±1.5(1.0) keV have been observed. Coincidence and γ-γ directional correlation measurements were performed with two NaI detectors, a fast coincidence system, and a multiparameter analyzer to record the data. The coincidence studies indicated levels at 616.2±0.5, 1255.6±0.6, and 1320.2±0.9 keV in ^{80}Kr, and 665.6±0.5 and 1477.6±1.6 keV in ^{80}Se. The experimental directional correlation coefficients of the 639.2–616.2-keV, 704.0–616.2-keV, and 812.0–665.6-keV cascades are $A_2=-(0.12\pm0.04)$, $A_4=+(0.38\pm0.10)$; $A_2=+(0.38\pm0.06)$, $A_4=+(1.28\pm0.18)$; and $A_2=+(0.29\pm0.13)$, $A_4=+(1.32\pm0.37)$, respectively. These values are compatible with spin assignments of 0^+ for the 1477.6-keV level in ^{80}Se, and of 2^+ and 0^+ for the 1255.6- and 1320.2-keV ^{80}Kr levels, respectively.

I. INTRODUCTION

In recent years there has been considerable interest in the low-lying states of spherical even-even nuclei. In many cases these states have been found to have a collective nature in that they possess many of the properties of quadrupole surface vibrations about a spherical equilibrium shape. Particular interest has centered around the 0^+, 2^+, and 4^+ members of the "2-phonon state." However, it is only in a very limited number of cases that all three members of the triplet have been identified. In most cases it is the 2^+ and 4^+ members that are observed. Even in the cases where the 0^+ state is seen, it is not always clear that it has the same character as the other two members of this triplet. It has been pointed out by Kisslinger[1] that if one includes in perturbation theory the parts of the interaction which are dropped in the quasiparticle random-phase approximation, it is found that the 0^+ state is affected much more than the other states. Numerous other investigators have dealt with the nature of these states at about twice the energy of the first 2^+ state in medium-weight even nuclei, but certainly the recent work of Kregar and Mihailovic[2] lends credence to the assertion that in some cases they cannot be described as members of a vibrational triplet. They[2] show that the second 0^+ states of several even nuclei in the germanium-selenium region can be interpreted by means of the nonadiabatic model of Davydov[3] as belonging to the

* Work supported in part by a grant from the National Science Foundation.

† On leave from the Technical University, Delft, Netherlands.

‡ Research contract sponsored by the U. S. Atomic Energy Commission under contract with the Union Carbide Corporation.

[1] L. S. Kisslinger, in *Internal Conversion Processes*, edited by J. H. Hamilton (Academic Press Inc., New York, 1966), p. 285.

[2] M. Kregar and M. V. Mihailovic, Nuklearni Institut Jozef Stefan, Ljubljana (Yugoslavia), Report No. R-484, 1966 (unpublished).

[3] A. S. Davydov, Nucl. Phys. **24**, 682 (1961).